Instabilities in the bottom boundary layer reduce boundary layer arrest, allowing cross-isobath spread of downwave flows and ventilating the boundary layer.

James M. Pringle

jpringle@unh.edu

University of New Hampshire

https://orcid.org/0000-0003-0031-5013

2/4/2021

Key points:

1. Instabilities in the bottom boundary layer prevent the arrest of the bottom boundary layer for flows in the Kelvin wave direction.
2. The prevention of bottom boundary layer arrest allows along-isobath flows to cross-isobaths, and allows slope flows to more effectively drive shelf flows.
3. Instabilities in the bottom boundary layer transport water from the bottom boundary layer into the stratified interior along isopycnals for flows in the Kelvin wave direction.

Abstract: An along-isobath current in stratified waters leads to a bottom boundary layer. In models with no alongshore variation, cross-isobath density transport in this bottom boundary layer reduce the velocity in the bottom boundary layer via thermal wind, and thus the bottom friction experienced by the current above the boundary layer – this is bottom-boundary-layer arrest.

If, however, alongshore variation of the flow is allowed, the bottom boundary layer is baroclinically unstable. We show with high resolution numerical models that these instabilities reduce this arrest and allow bottom friction to decelerate the flow above the bottom boundary layer when the flow is in the Kelvin wave direction (so that the bottom Ekman transport is downwelling). Both the arrest of the bottom boundary layer and the release from this arrest are asymmetric; the friction experienced by flows in the direction of Kelvin-wave propagation (downwave) is much greater than flows in the opposite direction.

The strength of the near bottom currents, and thus the magnitude of bottom friction, is found to be governed by the destruction of potential vorticity near the bottom balanced by the offshore along-isopycnal transport of this anomalous potential vorticity. A simple model of this process is created and used to quantify the magnitude of this effect and the resulting reduction of arrest of the bottom boundary layer. It is shown that the instabilities allow along-isobath flows to spread across isobaths and move boluses of weakly stratified bottom water into the stratified interior.

Plain Language Summary: It has long been thought that alongshore shore flows over the shelf and slope will, over time, change the cross-shelf distribution of salt and temperature near the bottom such that the flow at the bottom is small. This reduction in near-bottom flow reduces the friction between the alongshore flows and the bottom, in theory allowing the water to flow forever along the coast. This work shows, instead, that this cessation of flow near the bottom does not happen. Building on existing understanding of how the near bottom flow can break up into eddies, this work quantifies how much friction the alongshore flow feels, and finds it is greater than had been understood when the flow has the coast on its right in the Northern Hemisphere, and on its left in the southern Hemisphere. The greater friction, and the eddies created near the bottom, allow the deep ocean flows near the coastal ocean to drive alongshore flow on the shallow coastal ocean, and also take fluid from near the bottom and inject it into the deep ocean. Both of these effects couple the deep ocean to the shelf.

Index Terms:4568, 4562,4512

Keywords: Bottom boundary layer, Baroclinic Instabilities, Boundary Layer Arrest

1 Introduction

Garrett et al. (1993) and the references therein describe how an alongshore uniform along-isobath flow over a sloping bottom in a rotating stratified fluid leads to cross-isobath density transport. This transport would set up a cross-isobath buoyancy gradient which would lead to vanishing flows at the bottom – bottom boundary layer (BBL) arrest. The arrest of the near-bottom flow would eliminate the effect of bottom friction on flows higher in the water column, and Chapman (2002) found that the deceleration of an unforced along-isobath flow would be halted by the boundary layer arrest. Chapman and Lentz (1997) found that the bottom-boundary arrest would prevent an along-slope current flowing in the direction of Kelvin wave propagation (hereafter downwave) from spreading indefinitely across the shelf. Brink (2012) found that the effects of stratification and BBL arrest on limiting cross-isobath spread of alongshore flows became important as the slope Burger number exceeds roughly 0.2. BBL arrest prevents slope flows from driving shelf flows by preventing the frictional dissipation of relative vorticity in the overlying flows, a mechanism which allows flows to cross isobaths (e.g. Csanady, 1978).

These prior results did not focus on instabilities of the sloping isopycnals in the BBL, though the presence of isopycnal slope indicates the presence of available potential energy which could be released by an instability (Stone, 1970). Sloping isopycnals which intersect the bottom can be baroclinically unstable (Blumsack & Gierasch, 1972), and this instability persists in the presence of strong frictional effects (K. Brink & Cherian, 2013), and even be driven by them (McWilliams, 2016). Recent work has explicitly examined the linear stability of an arrested BBL, and found that it is unstable, with instability fast compared to the arrest scale for currents downwave directions, and slower growing instabilities for flows in the upwave sense (Wenegrat et al., 2018; Wenegrat & Thomas, 2020). Flows in the downwave sense lead to downwelling in the BBL, upwave flows to upwelling.

A pair of models is used to understand how the development of finite amplitude instabilities in the BBL can greatly reduce the arrest of the BBL. In particular, the magnitude of the near bottom velocity (and thus bottom friction) that persists despite the arrest mechanisms is estimated as a function of slope Burger number bottom, friction, stratification and alongshore flow strength. The results of this work is used to estimate how finite amplitude instability in the BBL can increase coupling between slope and shelf currents, at least for downwave slope currents (Gula et al. (2016) discusses upwave). The focus is on BBL arrest and instability within and closely above the BBL; sub-mesoscale motions caused by the separation of the BBL from the bottom at topographic variation is not examined (e.g. Gula et al., 2014; Molemaker et al., 2014). The same BBL instability mechanism that reduces arrest also ventilates the BBL, pushing boluses of weakly stratified bottom water into the stratified interior.

2 Methods: The primitive equation numerical model

To understand the role of stratification, friction and instability processes in decelerating an along-isobath flow over a sloping bottom, the deceleration of an initially barotropic current in a stratified, alongshore periodic ocean is examined. The fundamental approach is similar to Chapman (2002), but with a model domain that is both much more highly resolved and allows alongshore variation in the flow.

The deceleration of the flow by the bottom friction is caused by bottom stress. Because the prior literature uses both linear and quadratic drag laws, and because depending on the system being modeled, results for both a quadratic drag law

$$\vec{\tau}_{bot} = C_d \rho_0 \, \vec{u}_{bot} \cdot |\vec{u}_{bot}| \tag{1}$$

and a linear drag law

$$\vec{\tau}_{bot} = r \rho_0 \vec{u}_{bot} \tag{2}$$

will be given. $\vec{u}_{bot}$ is the velocity in the numerical model grid-point nearest to the bottom.

The deceleration of the alongshore current is examined with the Regional Ocean Modeling System (ROMS, Moore et al., 2011). The domain is 200 km across the shelf and 400 km along the shelf, with (except where specified) an alongshore resolution of 500 m. Some parameter sets are re-run with no alongshore variation.

In the development below, it is found that the bottom slope is an important parameter; to make scaling easier it is kept constant in the middle portion of the domain. The decay timescale of the alongshore flow is proportional to 1/depth, and to reduce the effect of the cross-isobath divergence of the cross-isobath flux of momentum we wish to have a relatively weak cross-shelf gradient in the alongshelf flow. To do this, and to roughly model the continental slope, the depth of the ocean is given by a hyperbolic tangent (for a nearly constant slope over the middle part of the domain) and is offset by a large constant (to reduce the factional depth change):

$$H(x) = H_0 + \alpha W \ \tanh\left(\frac{x - x_{pivot}}{W}\right) \tag{3}$$

where H_0 is the depth offset, α is the bottom slope, W is the width of sloping region, and x_{pivot} is the location where the depth is always equal to H_0 (Figure *1*). For model runs presented in this paper, H_0=600 m, W=30 km and x_{pivot}=100 km. The bottom slope is varied by run, and an example of the geometry is shown in figure 1. There are walls at x=0 and 200 km.

At the shallow (x=0 km) and offshore (x=200 km) boundaries, there is a 20km wide region in which the density structure is relaxed back to the initial structure; this damps the effect of Ekman pumping at the boundaries, preventing the formation of jets which, when they become unstable, can contaminate the interior portion of the model domain which are of interest. The timescale of decay is 0.25 day at the boundary and increases to infinity 20km from the boundary.

The initial state of the model is a uniform stratification N_0 and a spatially uniform alongshore geostrophic velocity in balance with an alongshore surface pressure gradient. There is no surface wind or buoyancy forcing, so the model spins down from this initial condition. 45 vertical levels are used, and to preserve resolution in the BBL, the following vertical coordinate parameters are chosen: $V_{transform}$=2, $V_{stretching}$=4, $\theta_s = 2.0, \theta_b = 4.0$ and T_{cline}=300 m (Shchepetkin & McWilliams, 2005). The base case bottom friction is r=$5 \times 10^{-4}\ m\ s^{-1}$ for linear friction and $C_d = 1.0 \times 10^{-3}$ for a quadratic drag law. The horizontal friction is biharmonic along s-coordinate surfaces with a magnitude of $2.38 \times 10^5\ m^4\ s^{-1}$. Halving the horizontal friction has no effects on the results presented here. When the horizontal resolution is changed, the horizontal friction is also changed to keep the damping timescale for $2\Delta x$ features constant. Vertical mixing is parameterized by the $k-\epsilon$ Generic Length Scale Mixing scheme (Warner et al., 2005) with the default ROMS parameters except with the background turbulent kinetic energy changed to match Warner et al. (2005) (KMIN=10^{-10} kg m^{-1} s^{-2} in the model) to provide reasonable background diffusivity at large Richardson number and to prevent rapid dissipation of background stratification.

3 Results: The model spindown

The spindown of the alongshore currents is examined in a series of model runs with varying parameters; guided by the existing literature on BBL arrest (K.H. Brink, 2012; D. C. Chapman, 2002), the spindown at the center of the slope of an initially spatially uniform velocity of 30 cm s^{-1} is shown (Figure *2*) for flows in the upwave and downwave direction for several values of the Slope Burger number

$$S = \frac{N_0}{f}\frac{\partial H}{\partial x} \tag{4}$$

In these runs, the initial stratification N_0 = $5\text{x}10^{-3}$ s^{-1} and f=10^{-4} s^{-1} and S is varied by altering the maximum bottom slope $\partial H/\partial x$. In the two-dimensional runs (the dashed lines of Figure 2) the deceleration ceases for larger values of S, and the deceleration is noticeably less for the upwave then downwave flows. These results are consistent with the boundary layer arrest literature cited above.

In the model runs with alongshore variation (the solid lines in the figure), the deceleration does not come to a halt in the downwave case. With alongshore variation, the dependence on S is complex. Deceleration is less with greater S as would be expected, but the difference between the alongshore varying and alongshore uniform runs also increases with greater S. In all cases the downwave flows decelerate faster than the upwave flows. Because these results indicate that the effect of allowing alongshore variation is more pronounced on the deceleration of the downwave flow, the focus below is on downwave flows.

In alongshore averaged fields (Figure 1) for the S=0.5 runs, the differences between the runs with and without alongshore variation are clear. Five days into the model run, a thick and well mixed BBL develops where downwelling bottom Ekman flows moves less-dense water under more dense water; the scale of the BBL is consistent with the existing literature (Garrett et al., 1993; Trowbridge & Lentz, 1991). There is a cross-shelf instability in the BBL for the first few days consistent with the symmetric instability discussed by Allen and Newberger (1998); but it quickly disappears when instabilities with alongshore variation grow. The suppression of symmetric instability by subsequent baroclinic instability has been seen in similar systems (e.g. K. H. Brink, 2015; Haine & Marshall, 1998). Within a few days there is alongshore variation in the alongshore velocity field in the BBL (Figure 1 bottom panels). By day 20, the deceleration of the along-isobath flows is noticeably different between the two- and three-dimensional cases, and the BBL has restratified in the latter case. By day 55 the instabilities are still bottom trapped but have extended horizontally offshore. The eddy processes in the downwave case are notably similar to the downwelling relaxation described in Brink (2015), and the restratification of the BBL is essentially similar to that described in Callies (2018).

To illustrate the evolution of the BBL instabilities, and their offshore progress with time, Figure 3 shows the evolution of a passive tracer in the S=0.5 case. The passive tracer is initialized so that its value is equal to the isobath depth it is over – so a tracer with a value of 630 started over the 630m isobath. The instability starts with small amplitude and a relatively small alongshore lengthscale. Over time, the alongshore length scale and offshore extent of the instability grows. In the bottom panels of Figure 1 the alongshore variability is seen to be largely trapped to the BBL.

3.1 Bottom boundary layer instabilities and the stratified interior

The instabilities restratify the BBL (e.g. Wenegrat et al., 2018). This restratification fundamentally alters the penetration of water near the bottom into the interior by reducing the small-scale turbulent diapycnal mixing of water (e.g. Perlin et al., 2018). At the same time, the eddies driving the restratification transport water horizontally away from the bottom, allowing communication of water properties from the near bottom into the geostrophic interior. In Figure 3, BBL eddies can be seen moving the tracer away from the boundary. As one would expect from work with dense water overflows (Yankovsky & Legg, 2018), localized surface cooling (David C. Chapman & Gawarkiewicz, 1997; Visbeck et al., 1996) and work on parameterization of mesoscale eddy fluxes (Gent & McWilliams, 1990 and the vast literature which grew from it), this eddy mixing away from the BBL tends to mix water more along isopycnal surfaces than across them. This is significantly different then the mixing that would be expected in a weakly stratified turbulent BBL, which mixes water across density classes in the turbulent BBL but also keeps the BBL isolated from the stratified waters above by the lack of turbulent mixing across the stratification above the BBL.

To examine the processes that mix water from the BBL into the stratified interior, a simulation of the linear friction base case, S=0.5, is conducted starting from day 15 of the model integration, after eddies have developed. Tracer is inserted into the model within 50m of the bottom between the 4.75 and 5.75°C isotherms (in this constant salinity model, isotherms are isopycnals). In Figure 4, the evolution of the tracer is shown over 45 days. As seen in other studies, the large majority of the mixing of tracer away from the BBL is along isopycnals, with little diapycnal mixing. The eddies pull the tracer 40km into the interior in 45 days.

When the near bottom flow is downwave, dissipation and mixing near the bottom produces water with greatly reduced Ertel Potential Vorticity (hereafter PV), and when the flow is upwave, upslope advection of density and diapycnal processes generates stratified water with larger PV (Benthuysen & Thomas, 2012). The eddies generated by the BBL instabilities then move the anamolous PV into the interior – in Figure 5A the value of the PV on the 5.25°C isotherm is shown for the same time as the tracer in Figure *4*A; the tracer contours are overlain on the PV. Most of the anomalous PV has an anomalously low magnitude because the bottom flow is largely downwave. The contours of the tracer inserted at the bottom match the low-PV anomaly well, indicating that the weakly stratified low-PV water was produced near the bottom and then carried into the interior.

The low PV anomaly can be seen to be limited to the region near the slope where the isopycnals have bent downward to intersect the slope, reducing the stratification (Figure 5B). The eddies have a Rossby number less than 1 and the low-PV is associate with lower stratification. To lower the stratification, the isopycnals which are horizontal in the interior must be tilted downward to intersect the slope, increasing the vertical spacing between the isopycnals. This downward tilt of the isopycnals sets up horizontal density gradients which, through thermal wind, reduce the near bottom alongshore velocity and reduces (though does not eliminate) the bottom drag on the overlying alongshore flow. In the development below, the BBL is defined as the region of low PV near the bottom.

3.2 A reduced-physics model of the extent of BBL arrest for downwave flows

Given the results above, it is hypothesized that the along-isopycnal mixing of PV by geostrophic eddies away from the bottom, and the subsequent restratification and reduction of horizontal density gradients in the BBL, is the mechanism reducing the BBL arrest. To test this, a "reduced physics" model is created which in which the evolution of PV near the sloping bottom is governed by the anomalous PV generated at the bottom and the transport of that PV anomaly by geostrophic eddies along isopycnals into the interior. If the reduced-physics model compares well to the solutions in the full primitive-equation model, it will support the hypothesis.

In the following derivation, it is assumed that all isopycnals that exist in the low-PV region above where the modeled isopycnal intersects the bottom also intersect the bottom where conditions (e.g. bottom slope, alongshore currents) are similar. This allows the further assumption that the cross-slope gradients in stratification, boundary layer thickness, horizontal density gradients and velocity are weak. This is defensible in the systems shown above, where the bottom slopes in the region of interest are nearly constant, the initial stratification is uniform, and the fractional depth changes are limited by the relatively deep water modeled. It limits the applicability of this model in cases where the region of high stratification is relatively thin, or where the bottom slope changes quickly across the shelf. In particular, the model cannot be directly applied to the shelf-break front intersecting the bottom near the shelf-break.

In this model, the along-isopycnal transport of PV is caused by eddies created by BBL instabilities. The flux of the PV q has been successfully modeled as a diffusive process with a diffusivity A_h that scales as the product of the length scale L_{eddy} of the eddy, a velocity scale V_{eddy} and a constant efficiency factor C_e (e.g. David C. Chapman & Gawarkiewicz, 1997; Spall, 2011; Visbeck et al., 1997):

$$A_h = C_e L_{eddy} V_{eddy} \tag{5}$$

and

$$\frac{\partial q}{\partial t} = A_h \frac{\partial^2 q}{\partial x^2} \tag{6}$$

The model equation is written in terms of the cross-shelf distance x and q is evaluated on an isopycnal; because the vertical excursion of the isopycnals is small relative to the horizontal length scales, there is no important difference between the along-isopycnal distance in the two-dimensional model and the cross-shelf coordinate x. The initial condition of our model system is uniform alongshore flow and stratification N_0^2, so the initial PV (and the PV in the interior) is

$$q = \omega_a \cdot \nabla b = (f\hat{\boldsymbol{z}} + \nabla \times \boldsymbol{u}) \cdot (\nabla b) = f N_0^2 \tag{7}$$

where b is the buoyancy anomaly $b = -g(\rho - \rho_0)/\rho_0$.

The lengthscale of the eddies doing the mixing is assumed to scale as the internal radius of deformation in the BBL (e.g. Spall, 2011; Wenegrat et al., 2018):

$$L_{eddy} = \frac{N_{LPV}\delta_{LPV}}{f} \tag{8}$$

where N_{LPV} is the buoyancy frequency in the low-PV region near the bottom, and δ_{LPV} is the vertical extent of that region. The eddy velocity V_{eddy} is assumed to scale with the average geostrophic alongshore velocity of the BBL. The geostrophic alongshore velocity is in the BBL, V_{LPV}, is the overlying current V reduced by thermal-wind shear in the BBL:

$$V_{LPV} = V + (z + H - \delta_{LPV})\frac{1}{f}\frac{\partial b}{\partial x} \tag{9}$$

Both L_{eddy} and V_{LPV} depend on the horizontal and vertical buoyancy gradients in the BBL. The horizontal density gradient can be estimated from the vertical buoyancy gradient in the low-PV region N_{LPV}^2. Above the low-PV region, the PV remains the initial PV, and the stratification remains the initial stratification N_0^2. The buoyancy in both these regions is then (assuming b=0 at z=0 and a water depth H)

$$b = N_0^2 z \quad \text{for } z \geq -H + \delta_{LPV} \tag{10}$$

$$b = N_{LPV}^2 z + C \quad \text{for } z \leq -H + \delta_{LPV} \tag{11}$$

Setting the constant C so that the buoyancy b is continuous at the top of the low-PV region and taking the cross-shelf derivative of b gives the cross-shelf gradient in buoyancy in the bottom low-PV region:

$$\frac{\partial b}{\partial x} = (N_0^2 - N_{LPV}^2)\left(-\frac{\partial H}{\partial x} - \frac{\partial \delta_{LPV}}{\partial x}\right) \tag{12}$$

Because of the assumption that the dynamics of the low-PV region is locally uniform in the cross-shelf direction, $\frac{\partial \delta_{LPV}}{\partial x}$ is assumed to be zero.

To estimate N_{LPV}^2, q_{LPV} is written assuming balanced flow (e.g. Holmes et al., 2014) so that:

$$q_{LPV} \approx f N_{LPV}^2 \left\{1 + \frac{1}{f}\frac{\partial V_{LPV}}{\partial x} - \frac{1}{N^2}\left(\frac{\partial V_{LPV}}{\partial z}\right)^2\right\} \tag{13}$$

Equations (9), (12) and (13), along with the assumption that cross-shelf conditions are roughly constant ($\frac{\partial^2 b}{\partial x^2} = 0$ and $\frac{\partial \delta_{LPV}}{\partial x} = 0$) can be used to find

$$N_{LPV}^2 = \left(\frac{\frac{q_{LPV}}{f} + \frac{N_0^4}{f^2}\left(\frac{\partial H}{\partial x}\right)^2}{1 + \frac{N_0^2}{f^2}\left(\frac{\partial H}{\partial x}\right)^2}\right) = \left(\frac{\frac{q_{LPV}}{f} + N_0^2 S^2}{1 + S^2}\right) \tag{14}$$

Where S is the slope Burger number given the initial stratification from (4). From these, the average velocity in the BBL, V_{eddy}, and the geostrophic velocity at the bottom from which drag is calculated V_{bot} can be written:

$$V_{bot} = V + \frac{\delta_{LPV}}{f^2}(fN_0^2 - q_{LPV})\frac{\partial H}{\partial x} \quad (15)$$

$$V_{eddy} = V + \frac{\delta_{LPV}}{2f^2}(fN_0^2 - q_{LPV})\frac{\partial H}{\partial x} \quad (16)$$

Note that V is negative for downwave flows for this bathymetry. V, the current above the BBL, can be estimated by assuming that the depth averaged velocity $<V>$ is decelerated by the bottom drag

$$\frac{\partial < V >}{\partial t} = -\frac{1}{H}\frac{\tau_{bot}^{y}}{\rho_0} \quad (17)$$

and correcting for the difference between the depth averaged velocity and the velocity above the BBL caused by the velocity deficit in the BBL:

$$V = < V > + \frac{\delta_{LPV}}{2f^2 H}(fN_0^2 - q_{LPV})\frac{\partial H}{\partial x} \quad (18)$$

This treatment of V neglects the cross-shelf advection of alongshelf momentum; this is discussed in the supplementary information.

PV is conserved in the interior; the anomalous PV near the bottom is caused by the flux of low-PV from the boundary where the isopycnal being modeled intersects the bottom. This flux is created by the viscous dissipation of alongshore momentum, and is well described by Benthuysen and Thomas (2012) and Wenegrat and Thomas (2020). A derivation closely following their work is given in the supplementary information. The flux of PV normal to the boundary is (where θ is the angle of the bottom from horizontal and τ_{bot}^{y} is the alongshore bottom stress calculated from V_{bot} and a drag law):

$$J^n = \hat{k} \cdot \nabla b \times \boldsymbol{F} \approx N_{LPV}^2 \theta \frac{\partial}{\partial z}(\rho_0^{-1}\tau^y) \approx N_{LPV}^2 \theta \frac{\tau_{bot}^{y}}{\delta \rho_0} = N_{LPV}^2 \theta \frac{\tau_{bot}^{y}}{\delta_{LPV}\rho_0}\,. \quad (19)$$

The vertical length scale δ has in other work (e.g. Wenegrat & Thomas, 2020) been set to the vertical scale of the low-PV layer, which is called δ_{LPV}. The justification for this is unclear, both in the prior literature and to this author. This assumption would appear inconsistent with the assumption that the PV dynamics are primarily along-isopycnal, unless there is divergence of the flux of momentum carried by the eddies along isopycnals across the low-PV region. The justification for using δ_{LPV} remains an open question; however, it is seen below that (19) correctly predicts the flux of PV from the bottom.

The PV flux in (19) is normal to the bottom, but the model in (6) is written in the cross-shelf coordinate. To correct for this rotation, the flux into (6) must be divided by the bottom slope. At small slope angles, θ is approximately equal to the bottom slope, and the boundary condition on (6) at the slope is

$$A_h \frac{\partial q}{\partial x} = \frac{J^n}{\frac{\partial H}{\partial x}} \approx N^2 \frac{\tau_{bot}^y}{\delta \rho_0} \tag{20}$$

To close the model, the thickness of the low-PV region δ_{LPV} and the average PV in this region , q_{LPV} are needed. The height of the low-PV layer near the bottom, δ_{LPV} is the along-isopycnal lengthscale of the low-PV anomaly L_{LPV} multiplied by the bottom slope

$$\delta_{LPV} = L_{LPV} \frac{\partial H}{\partial x} \tag{21}$$

because the top-most isopycnal in the low-PV layer at a point x_0 has, by assumption, the same L_{LPV} and the same cross-slope change in depth as the isopycnal originating at x_o, since it depends on the PV flux along that isopycnal where it intercepts the bottom. By assumption, that flux is the same as at x_0. The size of the near-bottom low-PV region L_{LPV} is found from the solution to the eddy-flux model (6). It is the extent of the near-bottom region where the PV is less than $1 - \epsilon$ of the interior PV fN_0^2. The model results are not sensitive to the exact value of ϵ. The results below are for $\epsilon = 0.1$, but minimal changes are seen for 0.05. The mean potential vorticity of the low-PV region q_{LPV} is the average PV from the slope boundary of the model to L_{LPV} offshore. These definitions of L_{LPV} and δ_{LPV} are computationally robust and efficient, but their non-linearity and non-algebraic form are the chief impediment to an analytic treatment of this model.

This completes the simplified model for the evolution of the low-PV layer. This model is solved with a small Python code included in the supplementary information, and can be run on a laptop.

3.3 Evaluating the reduced-physics model of BBL arrest for downwave flows

The reduced physics model described above is compared to the full solution of the ROMS numerical circulation model over the 600m isobath (the "full" model), which is always at the center of the slope. This ensures that the assumption that conditions do not vary locally across-isobaths is met. Both models are run for S from 0.1 to 1.8, initial currents of 0.15 m/s to 0.6 m/s, linear friction of 5 and 2.5×10^{-4} m/s or quadratic drag of 0.5, 1.0 and 2.0×10^{-3}, and initial values of N of 5 and 10×10^{-3} s^{-1}; the details are given in table 1. In the simple model, there is a single free parameter, the eddy mixing efficiency C_e. This is set to 0.06, which is the value that gives the minimum sum of squared differences between the ratio of bottom velocity to surface velocity in the two models in the quadratic drag case. This value is about 4 times greater than the value found for high Richardson number eddies in the surface ocean (Visbeck et al., 1997).

The results from the full numerical circulation model and the simple model for the quadratic drag law are compared after a 30 day model integration (figure 6). They compare well (in the supplementary information an animation is given showing the time evolution of this figure over 60 days; the results are very similar over all these times). Panels A and B show the surface and bottom velocities scaled by the initial velocity. In both more positive values indicate either greater BBL shutdown or reduced drag coefficient, and there is good agreement between the models. Panel C compares the estimate of the thickness of the low-PV layer, and the comparison is similarly good.

Panel D of figure 6 is the most dynamically important of the results shown; it is the ratio of the bottom velocity to the surface velocity, γ, and is a measure of the BBL arrest. Smaller values indicate greater arrest, with 0 being full arrest and 1 being no arrest. The agreement of the two models is good, with a correlation of 0.9 and a clustering around the 1:1 line. There is a systematic error where smaller initial alongshore currents lead the simple model to under-predict the extent of arrest when compared to the full circulation-model (e.g. for the S=0.5 (red) points, follow the sequences ♠ ,♣ and ♥ or ▼, ▲ and ◀ for initial alongshore velocities of 0.15, 0.3 and 0.6 m/s, respectively, at different drag values). One reason for this is that the BBL eddy mixing is assumed to be instantly fully developed; but in the primitive-equation model it takes time for the instability to develop, with weaker flows taking more time to develop eddies. But overall, the agreement is good.

The results for the linear bottom friction are similar, though with a tendency for the simple model to overpredict the amount of BBL arrest when the bottom velocity is weak (Figure 7B and C). In part this is because there is greater frictional decay of the alongshore flow for the linear drag, since the spin down timescale does not increase as the currents weaken with linear friction, as it does for the quadratic drag law (note that the effective friction coefficient r in the quadratic drag case is $Cd|\vec{v}|$). This effect is especially pronounced over the flatter portions of the model domain on either side of the slope (figure 1), leading to stronger currents over the slope with much weaker flows on either side. This leads to a weak instability and a meandering in the current over the slope which extends throughout the water column, leading to near bottom alongshore flow and bottom drag. This meander is seen as a weak deviation of the alongshore flow from the mean alongshore flow even above the low-PV region in the bottom row of figure 1. This is a mechanism distinct from that discussed here.

The close correspondence of the results between the reduced-physics model and the primitive equation numerical circulation model confirms the relevance of the reduced-physics model; the dynamics of partial BBL arrest and evolution can, for downwave flows, be understood as the creation of anomalous PV at the bottom and its fluxing into the interior by eddies that arise in the unstable BBL.

3.4 The parameter dependence of the reduced physics model

The reduced physics model can now be used to examine the dynamics of partial BBL arrest of downwave flows. The focus is on a BBL arrest parameter γ, and on the quadratic drag law, as this drag law makes the results more directly comparable to recent work on BBL shutdown (e.g. K. H. Brink & Lentz, 2009).

Begin by assuming that the water depth above the BBL is very great, so that the alongshore flow is not decelerated by the bottom drag; this is an assumption commonly made in studying BBL dynamics (Benthuysen & Thomas, 2012; e.g. K. H. Brink & Lentz, 2009; MacCready & Rhines, 1993). This assumption removes a timescale from the analysis, as it makes the timescale of the decay of the alongshore flow infinite. The simple model then depends on a small number of quantities: the drag coefficient C_d; the un-varying alongshore velocity above the BBL, V; the near-bottom geostrophic velocity V_{bot}; the initial stratification N_0; the Coriolis parameter f; the bottom slope $\frac{\partial H}{\partial x}$; and the time since the model has started with depth-uniform velocity and depth-uniform stratification, t. These seven quantities in two units, length and time, would suggest from Buckingham-P theory that this system is governed by 5 non-dimensional parameters. However, earlier results (e.g. K. H. Brink & Lentz, 2009 and citations therein) suggest that some of these non-dimensional parameters can be combined to reduce the dimensionality of the system. C_d and $\frac{\partial H}{\partial x}$ are combined with the other parameters to make the scaled drag C_dN_0/f and the slope Burger number $S = \frac{N}{f}\frac{\partial H}{\partial x}$. The remaining non-dimensional parameters are N/f, the BBL arrest parameter $\gamma=V_{bot}/V$, and the nondimensional time ft.

I have not been able write the reduced-physics model analytically, because δ_{LPV} is calculated numerically from the solution to (6), and so it cannot yet be rigorously shown that γ can be written as a function of S, N/f, tf, and C_dN_0/f. However, numerical solutions to the reduced-physics model find that for infinite water depth, γ is constant for any oceanographically realistic set of S, N/f, tf, and C_dN_0/f even as the individual dimensional parameters (e.g. N and f) are varied. This is shown in figure 8, where in the infinite depth case γ is shown for S=1.0, N/f=50.0, tf=42.3, and C_dN_0/f=0.15 as the quantities f, N, and C_d are varied by an order of magnitude; γ is constant even as the dimensional parameters vary. Even in the finite depth case, where H=600m, γ varies by 10% or less as the dimensional parameters are varied by an order of magnitude. The infinite depth solution remains close to the finite depth solution when the timescale of the current spindown $H/(\gamma C_d V)$ is long compared to the timescale of evolution of the reduced-physics model.

These results strongly suggest that the non-dimensional parameters S, N/f, tf, and C_dN_0/f are sufficient to understand the BBL arrest in the limit of a steady overlying flow, and are a good guide to understanding the magnitude of BBL arrest in finite depth cases. γ is shown as a function S, tf, and C_dN_0/f in panels B-E of figure 8, with greater γ indicating less arrest.

The least arrest (γ close to 1) is seen where *S* or the non-dimensional drag C_dN_0/f are small. This is consistent with the timescale needed for arrest in a downwelling-favorable (downwave) flow, which becomes infinite as either of these parameters becomes small. Figure 8 panels B) to E) include a line marking where the non-dimensional time *tf* is equal to the equivalent time scale for BBL arrest given in Brink and Lentz (2009) for a system with no alongshore variation. Above and to the right of this line the Brink and Lentz timescale is less than the time the model has been run (though it should be noted that instabilities modify the solution significantly well before the Brink and Lentz timescale). The most arrest occurs when both *S* and the non-dimensional drag C_dN_0/f become larger, with bottom currents less then 20% of the overlying currents as *S* exceeds $\approx$1.5 and C_dN_0/f exceeds $\approx$0.15. In all cases, increased non-dimensional bottom slope and stratification (*S*) or increased non-dimensional bottom drag decrease γ and thus reduce the effect of bottom drag on the overlying flow. At the same time, the instabilities prevent BBL arrest and allow bottom drag long after Brink and Lentz would predict complete BBL arrest. The code of the reduced-physics model used to produce figure 8 are provided in the supplementary materials.

4 Discussion

A reduced-physics model of the evolution of the bottom boundary layer was created, based on a simple eddy mixing parameterization of the effect of the eddies created in the BBL and the observation that eddies flux PV anomalies created at the bottom boundary along isopycnals away from the boundary. This model compares well with a fully primitive-equation numerical model of a downwave flow over a slopping bottom, strongly supporting the ideas that these limited dynamics are sufficient to capture effects of stratification on the bottom drag of a downwave flow in a strongly stratified ocean over a sloping bottom. These specific results are limited to the case where the stratification at the bottom does not very greatly in the cross-shelf direction.

4.1 Implications for numerical modeling of slope systems

The instability processes involved can be simulated by a standard hydrostatic numerical ocean model, such as the ROMS model used above. However, to do this, the resolution of the model must be sufficient to resolve these instabilities, and this resolution is finer than typical in most large-scale or regional models of coastal systems.

Figure 9 shows the decay of along-isobath surface currents for S=0.5 and linear bottom friction for horizontal model resolutions of 250m to 2km, along with the solutions for flows without alongshore variation. For the coarse 2km resolution, the runs with alongshore variation and instability are similar to those with no alongshore variation and experience significant BBL arrest; it should be noted that even this 2km resolution exceeds or matches that of most existing regional models. It is only as resolution becomes finer that the model solution converges, and the solution has both BBL instability and enhanced drag on the alongshore flow.

The failure of the relatively coarse resolution models to accurate simulate the deceleration of the alongslope currents in models that do not resolve the instability processes in the BBL, and fact that the resolution of these failing models is comparable or finer than many models of the shelf/slope sea, suggests that efforts to parameterize the effects of BBL instabilities are necessary.

4.2 Cross-slope coupling of currents

In the linear, low Rossby number limit, for a flow along the slope to cross-isobaths and drive flows on the shelf something must cause the depth-averaged potential vorticity of flow, f/H, to change. In the arrested topographic wave (ATW) limit, an along-isobath jet can spread across isobaths because of the frictional dissipation of relative vorticity (Csanady, 1978). In the ATW limit, slope flows drive shelf flows, and these shelf flows increase in the downwave direction as the current spreads across the shelf. Chapman and Lentz (1997), hereafter CL97, included stratification and bottom boundary layer arrest into a similar analysis on an f-plane. CL97, like ATW, assumes alongshore lengthscales are greater than cross-shelf scales and does not allow instabilities. CL97 found that boundary layer arrest, by shutting down the flow at the bottom and thus bottom friction, prevented the jet from widening or dissipating. This left it to flow unchanged along isobaths. In their limit, a slope jet in stratified slope waters remains mostly confined to the slope, and does not drive large shelf flows. The contrast between CL97 and ATW leads to the hypothesis that when instabilities reduce BBL arrest, they will allow a downwave slope jet to spread across isobaths as it progresses downwave.

To test this hypothesis, an idealized numerical model run was created with ROMS, with 100km wide shelf with a bathymetric-slope of 10^{-3} and a 200km wide slope with a bathymetric slope of 10^{-2}. The stratification was such that S=0.5 over the slope, and the system was driven by a jet flowing in from the northern boundary between the shelfbreak and 75km farther offshore with a velocity of 0.60 m s^{-1} (Figure 10). The domain has an alongshore extent of 1200km, or roughly the along-coast distance from the Laurentian Channel to Cape Cod or from the northern part of the Gulf of Maine to Cape Hatteras. Because of this latitudinal extent, the model is run on a β-plane, with f=10^{-4} s^{-1} and β=1.6×10^{-11} $s^{-1}m^{-1}$. With the same domain and forcing, the model of CL97 was implemented, along with the ATW model. To match CL97, the linear bottom friction was 5.0×10^{-4} m s^{-1}.

The results of these models are shown 1000km downwave of the inflow in Figure 10. A significant fraction of the jet has moved both offshore to deeper isobaths and onto the shelf in all cases. In all but the ATW model, along-slope flow increases downwave because the flow remains somewhat along lines of constant *f/H*, and as the flow moves equatorward, these lines converge shoreward because of β, accelerating the flow. In the CL97 solution, there is much less broadening of the jet; because of BBL arrest, the flow ceases to spread across lines of constant f/H. The effects of the reduced BBL arrest in the ROMS model which allows BBL instabilities is evident on the shelf, where the flow is 50% to 100% greater than would be expected from CL97. The model with BBL instabilities is significantly closer to the ATW solution because the instabilities allow bottom drag on the along-isobath flow.

These results are consistent with the changes in jet dynamics expected with stronger bottom friction. This suggests that the instability-driven reduction of BBL arrest and associated bottom friction seen in Figure 10 are important to include in efforts to understand the dynamics of downwave jets along continental slope, such as the Labrador current and its equatorward extension and the Oyashio. In a recent study of the effect of gyre scale circulation on shelf flows, the strength of the bottom friction was found to be a key control on the ability of gyre-scale circulation to change coastal sea level (Wise et al., 2018). This suggests that BBL instability increase the influence of the gyre scale circulation on coastal sea level when the western boundary current is downwave, as is true in the sub-polar gyres and the equatorward extension of their western boundary currents.

4.3 Observing BBL non-arrest

Observations of boundary layer arrest on the shelf are sparse; of BBL instabilities more so. As seen in Figure 1, once the BBL becomes unstable, it becomes restratified even in the presence of along-isobath downwave flows which would be expected to continuously destroy the stratification . While the along-isobath current is flowing downwave, instabilities would be continuously fueled by the downslope Ekman transport's injection of potential energy into the density field – and would create enhanced variability in the along-isobath flow in the low-PV region relative to the more stratified waters above (e.g. Figure 1, bottom panels). Attempting to estimate bottom boundary layer dissipation of energy in the ocean Sen et al. (2008) and Wright et al. (2012) examined their current data for evidence of BBL shutdown and failed to find any evidence for it. Wright et al. (2012) found greater currents near the bottom than above. These are consistent with the predictions above – but neither effort controlled for the slope Burger number S. Callies (2018) studied the restratification of abyssal BBL by instabilities, compared his predictions to observed BBL stratification in the South Atlantic Ridge, and found good agreement.

A more easily observed indicator of BBL instabilities and arrest escape would be an increase in the frequency of boluses low PV, weakly stratified water in the otherwise stratified waters near the slope when the near-bottom flows are downwave, even while the BBL does not create a thick (e.g. comparable to the predictions of Chapman and Lentz (1997)) bottom mixed layer (e.g. figures *1* and 5; see also Wenegrat et al. (2018)). For example, the slope Burger number of coastal Peru at about 15°S during the late summer of 1977 was roughly 1.6. As part of the Coastal Ecosystem Upwelling Analysis program in coastal Peru from March to mid-May of 1977 (Kenneth H. Brink et al., 1978, 1979) two moorings were placed in the water column at a depth 121m (12km from the coast) and in 86m (4km from the coast) at about 15°S. The near bottom flows showed 7 to 12 day periods of downwave (negative/poleward) flow alternating with periods of upwave flows of shorter duration (2-5 days). The data are low-pass filtered with the pl33 filter (Beardsley et al., 1985) with a half-power point of 46 hours (Figure 11).

In CTD surveys taken along the mooring line, regions of well mixed water can be found away from the bottom or surface boundary layers; an example from the 19th of March 1977 is given in Figure 11, where a regions is marked as well mixed if there is a less than 0.01°C change in the vertical. These well mixed patches were smaller than the horizontal resolution of the CTD sections (roughly 6km), most were less than 10m thick, and nearly all less than 20m thick. Most of the well mixed patches were in the lower half of the water column. Unfortunately, the temporal resolution of the CTD data was insufficient to compare to the currents.

The temperature sensors on the moorings were widely spaced; for the mooring at 121m depth, the sensors were at 115, 100, 80, 59m and shallower (Figure 11). In an analysis (not shown) of stratification estimated between the bottom two instruments of each mooring, a strong association was found between downwave flows and relatively "well-mixed" bottom boundary layers as estimated by the relatively widely spaced current meters (between 115 and 100m in 121m depth, and 78 and 67m in 86m depth; a "mixed layer" is defined as a temperature difference <0.02°C; this is the strictest criterion which makes sense given the accuracy of the Anderaa current meters (K.H. Brink et al., 1978)). This is as would be expected for downwelling flows. However, interestingly, the "well-mixed" periods were intermittent even near the bottom during strong downwelling favorable flows. Over a two-day period the maximum frequency of time the water was well-mixed was less than 30% of the time at the shallow mooring, and likewise at the deeper mooring. This intermittency might be caused by the large vertical spacing of the sensors and their distance from the bottom. Or they might be due, as suggested by the modeling above, to the eddy-restratification of the bottom boundary layer.

Away from the bottom, in the next higher pairs of temperature sensors on both moorings, there is evidence of boluses of "well-mixed" water passing between the sensors. 1 percent of the time at the 86m depth mooring, between 46 and 67m, the water is "well-mixed." 6 percent of the time the water is "well-mixed" between the 80 and 100m sensors at the 121m mooring (Figure 11). These "well-mixed" periods were intermittent. Even over a one-day window, the peak frequencies of "well-mixed" water was about 30-50%. To compare the frequency of the mixed layer to the alongshore current, the alongshore velocity (filtered with a two-day average) at the second sensor above the bottom is correlated to the daily mixed layer frequency. Because the distribution of mixed layer frequency is very non-Gaussian, Kendall's τ, a non-parametric correlation coefficient, is used and the confidence calculation is adjusted for the large number of ties in the data (Daniel, 2000). The correlation between the alongshore velocity and the frequency of well-mixed water between 80 and 100m is -0.27, and -0.38 between 100m and 115m, both significant at the 95% level. The sign of the correlation is consistent with downwave flows leading to boluses of well mixed waters leaving the bottom boundary layer. The relatively low correlations and intermittency of mixed layers is consistent with kilometer scale filaments and boluses of relatively well mixed (low PV) waters of kilometer-scale horizontal extent surrounded by stratified waters being advected through the moorings by an alongshore velocity of O(0.1 to 0.2) m s^{-1} when the flow (averaged over eddies) is downwave.

Conclusions:

The BBL arrest suggested by Garret et al. (1993), Trowbridge and Lentz (1991), Chapman and Lentz (1997) and others is found to be reduced by baroclinic instabilities in the BBL when the flow is downwave. The downwave flow drives diabatic mixing which destroys PV in the bottom boundary layer (Benthuysen & Thomas, 2012), creating horizontal density gradients which become baroclinically unstable. The resulting eddy mixing stirs the low-PV water offshore, restoring stratification in the BBL and reducing the BBL arrest. Where boundary layer arrest is broken down by instabilities in the boundary layer, the overlying geostrophic flow remains frictionally coupled to the bottom. The resulting Ekman pumping can both slow the alongshore flows and allow them to spread across isobaths. This mechanism can enhance the coupling between downwave slope flows and the shelf, and lead to stronger flows on the shelf in the same direction as the slope flows and coupling shelves to the adjacent gyre scale circulation (Wise et al., 2018). The eddies created by the BBL instabilities mix water from the BBL nearly horizontally into the stratified interior, a potentially important mechanism for coupling the sediment/water interface into the stratified interior. Given that large scale ocean models currently have resolutions that fail to capture the effects of BBL instabilities (e.g. Figure 9), some parameterization of their dynamics, based on theory and validated by observations, is essential to understanding their broader impact.

A simple model has been created, and is provided in the supplementary information, which captures these processes and accurately predicts the extent of BBL layer arrest and the spread of low-PV water into the stratified interior.

The strength of the near bottom flows relative to overlying flow, and thus the strength of the drag on the overlying flows, is a function of the non-dimensional parameters $S=\frac{N}{f}\frac{\partial H}{\partial x}$, N/f, tf, and C_dN_0/f in the limit of an infinitely deep ocean or an overlying flow of fixed strength. In the limit of finite depth and a flow which decelerates due to drag, these results are still approximately true. The near bottom flow is greater (the arrest in the BBL is less) when the slope Burger number S is less or the non-dimensional drag $C_d N_0/f$ is less; the sensitivity to the other parameters is much less, for reasonable oceanographic values. These results suggest that BBL instability and reduced BBL arrest should be broadly important – for instance on the slope adjacent to the Mid-Atlantic Bight where the shelf and slope flows are downwave (Robinson & Brink, 2006), and the slope Burger numbers are moderate (Figure 12).

The direct observation of these relatively small scale and near bottom instabilities is challenging – but the predictions of near bottom instabilities, boluses of weakly stratified water horizontally adjacent to the BBL and stratified BBL's during downwave flow are consistent with observations (e.g. Stahr & Sanford, 1999 and citations within and above).

The description above of the impact of BBL instability on the stratification and flow near the bottom is incomplete; much remains to be done. Most importantly will be to express the simple model presented above in a more analytic formulation in order to more mechanistically understand the relation between the governing parameters and the velocity in the BBL. In particular, the reason the vertical length scale of stress-divergence in (19) can be expressed as the thickness of the low-PV region remains unclear. The simple model created above also assumes that the stratification and bottom slope are slowly changing in the cross-shelf direction, so that over a horizontal length scale $\delta_{LPV}\left(\frac{\partial H}{\partial x}\right)^{-1}$ the alongshore flow and stratification at the bottom remain relatively constant. This is not applicable where the thermocline intersects the bottom, leading to a thin region of enhanced S (e.g. the shelf/slope fronts seen in Figure 12.)

Nonetheless, the instabilities of the BBL have been shown to have impacts well outside of the bottom boundary layer, and are important in the coupling of the overlying stratified waters to the BBL, both for momentum and the injection of BBL water into the stratified interior. These small scale dynamics are usually missing in our larger scale models, be they conceptual, idealized or numerical.

Acknowledgements:

The analysis of the CUEA data from Peru was inspired by unpublished work of Kenneth Brink and Jane Huyer. Kenneth Brink and Steve Lentz read an early draft and gave comments which substantially altered the work. Leif Thomas and Jacob Wenegrat were generous with their time in helping explain their work. This work was funded by NSF Physical Oceanography OCE1459609. The model code for the reduced physics model described in the text is provided in the supplemental information.

Bibliography

Allen, J. S., & Newberger, P. A. (1998). On Symmetric Instabilities in Oceanic Bottom Boundary Layers. *Journal of Physical Oceanography*, *28*(6), 1131–1151. https://doi.org/10.1175/1520-0485(1998)028<1131:OSIIOB>2.0.CO;2

Beardsley, R. C., Limeburner, R., & Rosenfeld, L. K. (1985). *Introduction to CODE-2 Moored Array and Large-Scale Data Report in CODE-2: Moored Array and Large-Scale Data Report* (WHOI Technical Report No. 85–35). WHOI. Retrieved from https://darchive.mblwhoilibrary.org/bitstream/handle/1912/1641/WHOI-TR-85-35.pdf

Benthuysen, J., & Thomas, L. N. (2012). Friction and Diapycnal Mixing at a Slope: Boundary Control of Potential Vorticity. *Journal of Physical Oceanography*, *42*(9), 1509–1523. https://doi.org/10.1175/JPO-D-11-0130.1

Blumsack, S. L., & Gierasch, P. J. (1972). Mars: The effects of topography on baroclinic instability. *JAS*, *29*, 1081–1089.

Brink, K., & Cherian, D. A. (2013). Instability of an idealized tidal mixing front: Symmetric instabilities and frictional effects. *Journal of Marine Research*, *71*(6), 425–450.

Brink, K. H. (2015). Continental Shelf Baroclinic Instability. Part I: Relaxation from Upwelling or Downwelling. *Journal of Physical Oceanography*, *46*(2), 551–568. https://doi.org/10.1175/JPO-D-15-0047.1

Brink, K. H., & Lentz, S. J. (2009). Buoyancy Arrest and Bottom Ekman Transport. Part I: Steady Flow. *Journal of Physical Oceanography*, *40*(4), 621–635. https://doi.org/10.1175/2009JPO4266.1

Brink, Kenneth H., Allen, J. S., & Smith, R. L. (1978). A Study of Low-Frequency Fluctuations Near the Peru Coast. *Journal of Physical Oceanography*, *8*(6), 1025–1041. https://doi.org/10.1175/1520-0485(1978)008<1025:ASOLFF>2.0.CO;2

Brink, Kenneth H., Gilbert, W. E., & Huyer, A. (1979). Temperature sections along the C-line over the shelf off Cabo Nazca, Peru from moored current meters : 18 March-10 May 1977 and CTD observations, 5 March-15 May 1977. Oregon State University.

Brink, K.H. (2012). Buoyancy arrest and shelf–ocean exchange. *Journal of Physical Oceanography*, *42*(4), 644–658.

Brink, K.H., Smith, R. L. (Robert L., Halpern, D., & Oceanography, O. S. U. S. of. (1978). A compendium of time series measurements from moored instrumentation during the MAM ’77 phase of JOINT-II.

Callies, J. (2018). Restratification of abyssal mixing layers by submesoscale baroclinic eddies. *Journal of Physical Oceanography*, *48*(9), 1995–2010.

Chapman, D. C. (2002). Deceleration of a finite-width, stratified current over a sloping bottom: Frictional spindown or buoyancy shutdown?, *32(1)*, 336–352.

Chapman, David C., & Gawarkiewicz, G. (1997). Shallow convection and buoyancy equilibration in an idealized coastal polynya, *27*, 555–566.

Chapman, David C., & Lentz, S. J. (1997). Adjustment of Stratified Flow over a Sloping Bottom. *Journal of Physical Oceanography*, *27*(2), 340–356. https://doi.org/10.1175/1520-0485(1997)027<0340:AOSFOA>2.0.CO;2

Csanady, G. T. (1978). The Arrested Topographic Wave. *Journal of Physical Oceanography*, *8*(1), 47–62. https://doi.org/10.1175/1520-0485(1978)008<0047:TATW>2.0.CO;2

Daniel, W. (2000). *Applied Nonparametric Statistics* (2 edition). Australia; Pacific Grove, CA: Cengage Learning.

Garrett, C., MacCready, P., & Rhines, P. (1993). Boundary Mixing and Arrested Ekman Layers: Rotating Stratified Flow Near a Sloping Boundary. *Annual Review of Fluid Mechanics*, *25*(1), 291–323. https://doi.org/10.1146/annurev.fl.25.010193.001451

Gent, P. R., & McWilliams, J. C. (1990). Isopycnal mixing in ocean circulation models. *Journal of Physical Oceanography*, *20*(1), 150–155.

Gula, J., Molemaker, M. J., & McWilliams, J. C. (2014). Gulf Stream dynamics along the Southeastern U.S. Seaboard. *Journal of Physical Oceanography*. https://doi.org/10.1175/JPO-D-14-0154.1

Gula, J., Molemaker, M. J., & McWilliams, J. C. (2016). Topographic generation of submesoscale centrifugal instability and energy dissipation. *Nature Communications*, *7*, 12811.

Haine, T. W. N., & Marshall, J. (1998). Gravitational, Symmetric, and Baroclinic Instability of the Ocean Mixed Layer. *Journal of Physical Oceanography*, *28*(4), 634–658. https://doi.org/10.1175/1520-0485(1998)028<0634:GSABIO>2.0.CO;2

Hallberg, R., & Rhines, P. B. (2000). Boundary sources of potential vorticity in geophysical circulations. *Fluid Mechanics and Its Applications*, *58*, 51–66.

Haynes, P. H., & McIntyre, M. E. (1987). On the Evolution of Vorticity and Potential Vorticity in the Presence of Diabatic Heating and Frictional or Other Forces. *Journal of the Atmospheric Sciences*, *44*(5), 828–841. https://doi.org/10.1175/1520-0469(1987)044<0828:OTEOVA>2.0.CO;2

Holmes, R. M., Thomas, L. N., Thompson, L., & Darr, D. (2014). Potential Vorticity Dynamics of Tropical Instability Vortices. *Journal of Physical Oceanography*, *44*(3), 995–1011. https://doi.org/10.1175/JPO-D-13-0157.1

Lentz, S. J., & Chapman, D. C. (2004). The Importance of Nonlinear Cross-Shelf Momentum Flux during Wind-Driven Coastal Upwelling. *Journal of Physical Oceanography*, *34*(11), 2444–2457. https://doi.org/Article

MacCready, P., & Rhines, P. B. (1993). Slippery Bottom Boundary Layers on a Slope. *Journal of Physical Oceanography*, *23*(1), 5–22. https://doi.org/10.1175/1520-0485(1993)023<0005:SBBLOA>2.0.CO;2

McWilliams, J. C. (2016). Submesoscale currents in the ocean. *Proceedings of the Royal Society A: Mathematical, Physical and Engineering Sciences*, *472*(2189), 20160117.

Molemaker, M. J., McWilliams, J. C., & Dewar, W. K. (2014). Submesoscale Instability and Generation of Mesoscale Anticyclones near a Separation of the California Undercurrent. *Journal of Physical Oceanography*, *45*(3), 613–629. https://doi.org/10.1175/JPO-D-13-0225.1

Moore, A. M., Arango, H. G., Broquet, G., Powell, B. S., Weaver, A. T., & Zavala-Garay, J. (2011). The Regional Ocean Modeling System (ROMS) 4-dimensional variational data assimilation systems: Part I–System overview and formulation. *Progress in Oceanography*, *91*(1), 34–49.

Perlin, A., Moum, J. N., Klymak, J. M., Levine, M. D., Boyd, T., & Kosro, P. M. (2018). Organization of stratification, turbulence, and veering in bottom Ekman layers. *Journal of Geophysical Research: Oceans*. https://doi.org/10.1029/2004JC002641@10.1002/(ISSN)2169-9291.COAST1

Robinson, A. R., & Brink, K. H. (2006). *The Sea, Volume 14B, The Global Coastal Ocean: Interdisciplinary Regional Studies and Syntheses*. Harvard University Press.

Sen, A., Scott, R. B., & Arbic, B. K. (2008). Global energy dissipation rate of deep-ocean low-frequency flows by quadratic bottom boundary layer drag: Computations from current-meter data. *Geophysical Research Letters*, *35*(9). https://doi.org/10.1029/2008GL033407

Shchepetkin, A. F., & McWilliams, J. C. (2005). The regional oceanic modeling system (ROMS): a split-explicit, free-surface, topography-following-coordinate oceanic model. *Ocean Modelling*, *9*(4), 347–404.

Spall, M. A. (2011). On the role of eddies and surface forcing in the heat transport and overturning circulation in marginal seas. *Journal of Climate*, *24*(18), 4844–4858.

Stahr, F. R., & Sanford, T. B. (1999). Transport and bottom boundary layer observations of the North Atlantic Deep Western Boundary Current at the Blake Outer Ridge. *Deep Sea Research Part II: Topical Studies in Oceanography*, *46*(1), 205–243. https://doi.org/10.1016/S0967-0645(98)00101-5

Stone, P. H. (1970). On non-geostrophic baroclinic stability: Part II. *JAS*, *27*, 21–726.

Taylor, J. R., & Ferrari, R. (2010). Buoyancy and wind-driven convection at mixed layer density fronts. *Journal of Physical Oceanography*, *40*(6), 1222–1242.

Trowbridge, J. H., & Lentz, S. J. (1991). Asymmetric Behavior of an Oceanic Boundary Layer above a Sloping Bottom, *21*, 1171–1185.

Visbeck, M., Marshall, J., & Jones, H. (1996). Dynamics of isolated convective regions in the ocean, *26*, 1721–1734.

Visbeck, M., Marshall, J., Haine, T., & Spall, M. (1997). Specification of eddy transfer coefficients in coarse resolution ocean circulation models, *27*, 381–402.

Warner, J. C., Sherwood, C. R., Arango, H. G., & Signell, R. P. (2005). Performance of four turbulence closure models implemented using a generic length scale method. *Ocean Modelling*, *8*(1), 81–113. https://doi.org/10.1016/j.ocemod.2003.12.003

Wenegrat, J. O., & Thomas, L. N. (2020). *Centrifugal and symmetric instability during Ekman adjustment of the bottom boundary layer* (preprint). EarthArXiv. https://doi.org/10.31223/osf.io/cgsk8

Wenegrat, J. O., Callies, J., & Thomas, L. N. (2018). Submesoscale Baroclinic Instability in the Bottom Boundary Layer. *Journal of Physical Oceanography*, *48*(11), 2571–2592. https://doi.org/10.1175/JPO-D-17-0264.1

Wise, A., Hughes, C. W., & Polton, J. A. (2018). Bathymetric Influence on the Coastal Sea Level Response to Ocean Gyres at Western Boundaries. *Journal of Physical Oceanography*, *48*(12), 2949–2964. https://doi.org/10.1175/JPO-D-18-0007.1

Wright, C. J., Scott, R. B., Furnival, D., Ailliot, P., & Vermet, F. (2012). Global Observations of Ocean Bottom Subinertial Current Dissipation. *Journal of Physical Oceanography*, *43*(2), 402–417. https://doi.org/10.1175/JPO-D-12-082.1

Yankovsky, E., & Legg, S. (2018). Symmetric and Baroclinic Instability in Dense Shelf Overflows. *Journal of Physical Oceanography*, *49*(1), 39–61. https://doi.org/10.1175/JPO-D-18-0072.1

Table 1: Key to model run symbols.

Color	Slope Burger #	f
●	S=0.1	10^{-4}
●	S=0.3	10^{-4}
●	S=0.5	10^{-4}
●	S=0.7	10^{-4}
●	S=0.9	10^{-4}
●	S=1.2	0.5×10^{-4}
●	S=1.5	0.5×10^{-4}
●	S=1.8	0.5×10^{-4}

Marker	Initial Velocity	Drag Coefficient	Initial Buoyancy Frequency
▾	0.15 ms^{-1}	5e-04	5e-03 s^{-1}
▴	0.30 ms^{-1}	5e-04	5e-03 s^{-1}
◂	0.60 ms^{-1}	5e-04	5e-03 s^{-1}
♠	0.15 ms^{-1}	1e-03	5e-03 s^{-1}
♣	0.30 ms^{-1}	1e-03	5e-03 s^{-1}
♥	0.60 ms^{-1}	1e-03	5e-03 s^{-1}
★	0.15 ms^{-1}	2e-03	5e-03 s^{-1}
×	0.30 ms^{-1}	2e-03	5e-03 s^{-1}
✶	0.60 ms^{-1}	2e-03	5e-03 s^{-1}

Marker	Initial Velocity	Bottom Friction r	Initial Buoyancy Frequency
▾	0.15 ms^{-1}	2.5e-04 ms^{-1}	5e-03 s^{-1}
★	0.15 ms^{-1}	2.5e-04 ms^{-1}	1e-02 s^{-1}
▴	0.30 ms^{-1}	2.5e-04 ms^{-1}	5e-03 s^{-1}
×	0.30 ms^{-1}	2.5e-04 ms^{-1}	1e-02 s^{-1}
▾	0.60 ms^{-1}	2.5e-04 ms^{-1}	5e-03 s^{-1}
✶	0.60 ms^{-1}	2.5e-04 ms^{-1}	1e-02 s^{-1}
♠	0.15 ms^{-1}	5.0e-04 ms^{-1}	5e-03 s^{-1}
⬟	0.15 ms^{-1}	5.0e-04 ms^{-1}	1e-02 s^{-1}
♣	0.30 ms^{-1}	5.0e-04 ms^{-1}	5e-03 s^{-1}
¤	0.30 ms^{-1}	5.0e-04 ms^{-1}	1e-02 s^{-1}
♥	0.60 ms^{-1}	5.0e-04 ms^{-1}	5e-03 s^{-1}
◆	0.60 ms^{-1}	5.0e-04 ms^{-1}	1e-02 s^{-1}

The parameters used in the full numerical model runs, both with linear and quadratic bottom drag, along with a key to the symbols and colors used in the figures to represent these model runs.

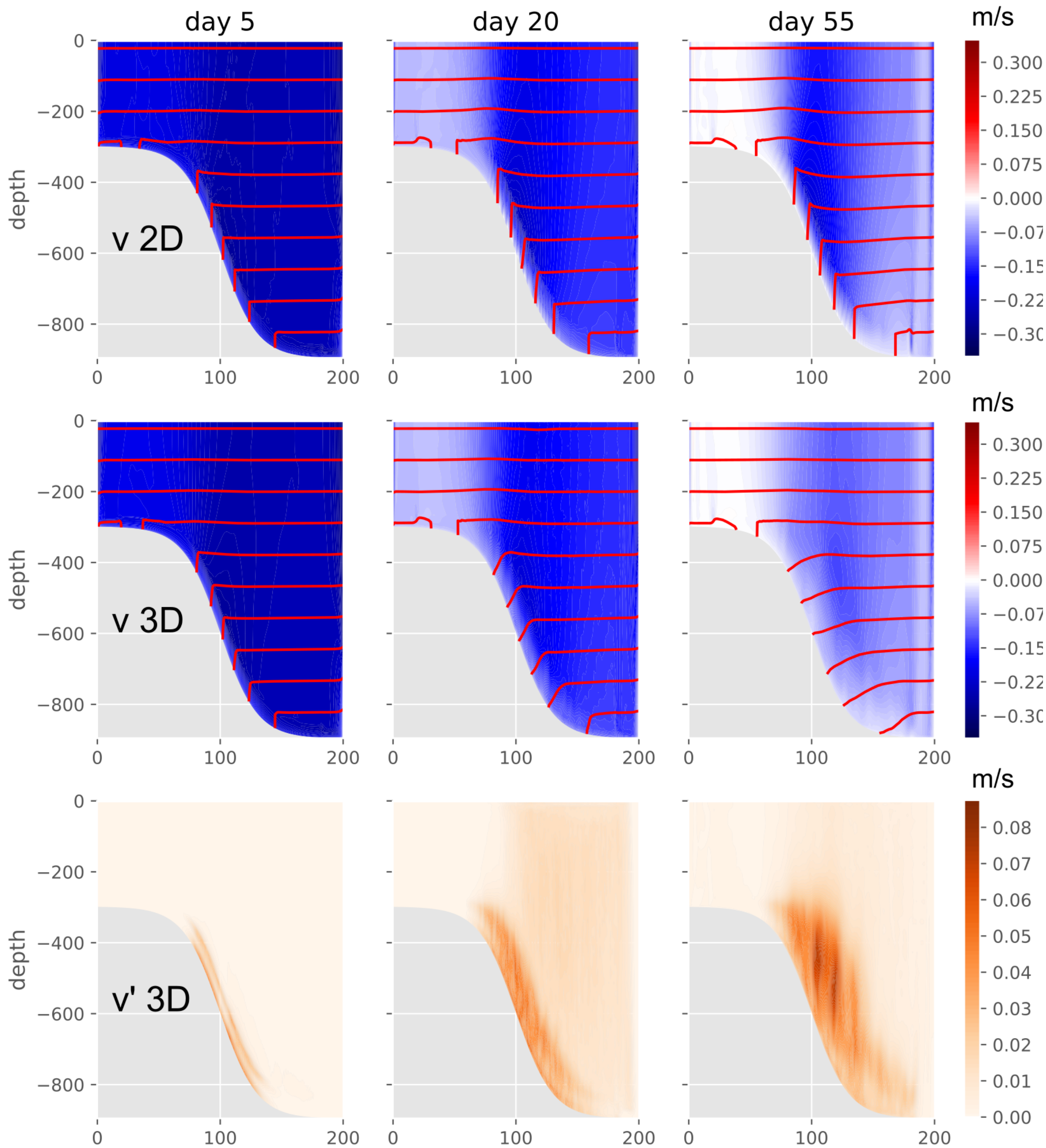

Figure 1: Top row: the alongshore velocity (colors) and isopycnals (red) for days 5, 20 and 55 of the case with no alongshore variation and an initial downwave-ward flow. Middle row: the alongshore flow and isopycnals for the same days in the case with alongshore variation. Bottom row: the standard deviation from the alongshore mean of the alongshore velocity (v’) for the case with alongshore variation.

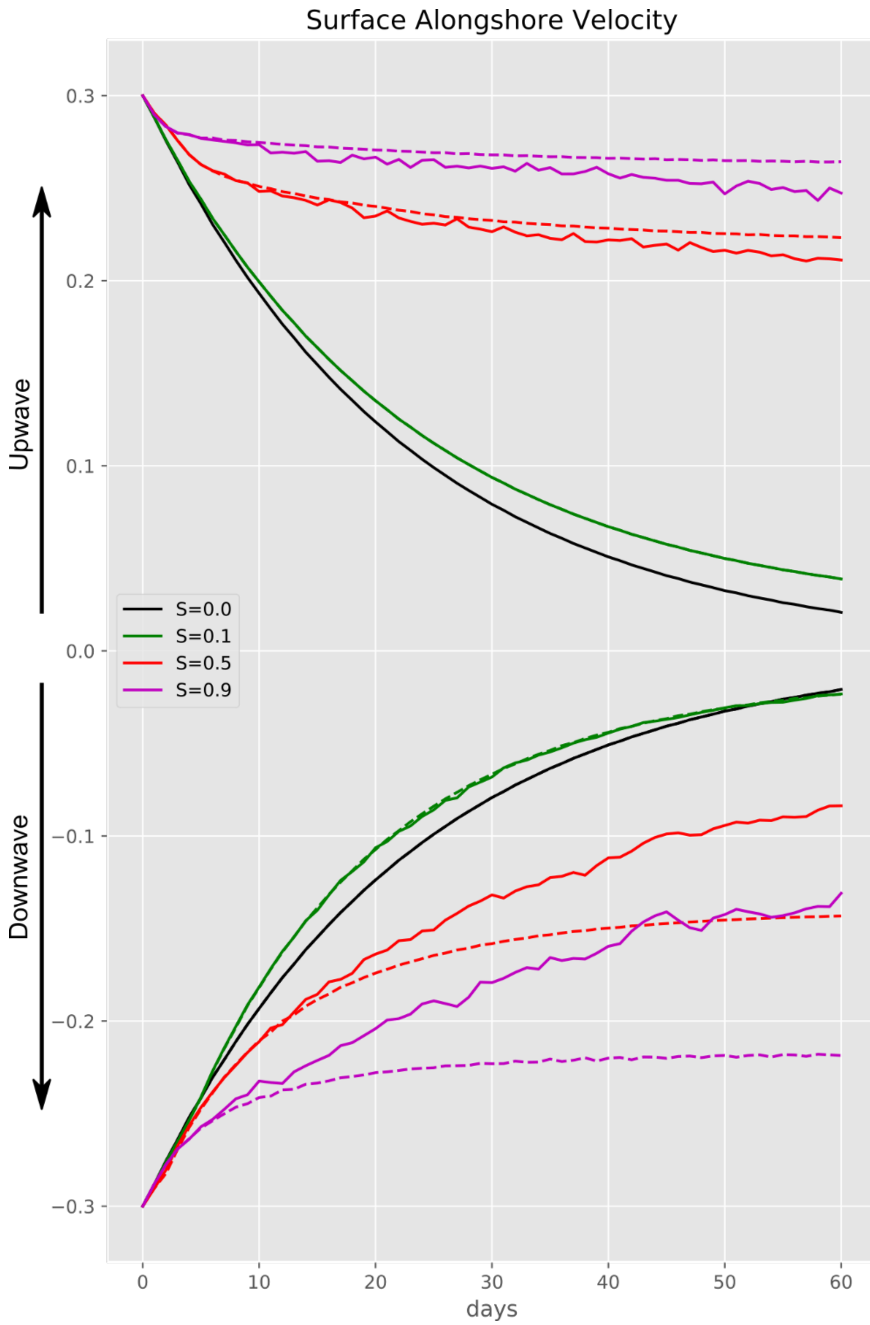

Figure 2: The surface velocity 100km offshore over sixty days for 12 model runs which all start with an alongshore velocity of 0.3 m/s. The dashed lines are for a model with no alongshore variation. The solid lines are for model runs which allow alongshore variation. There are models for a Slope Burger number of 0.0, 0.1, 0.5 and 0.9, and the initial velocity is oriented in either the upwave (positive, poleward) or downwave (negative, equatorward). For these runs, N=5×10^{-3} s^{-1}, r= 5×10^{-4} m s^{-1} and $f = 1 \times 10^{-4}$ s^{-1}, and S is altered by altering the bathymetry.

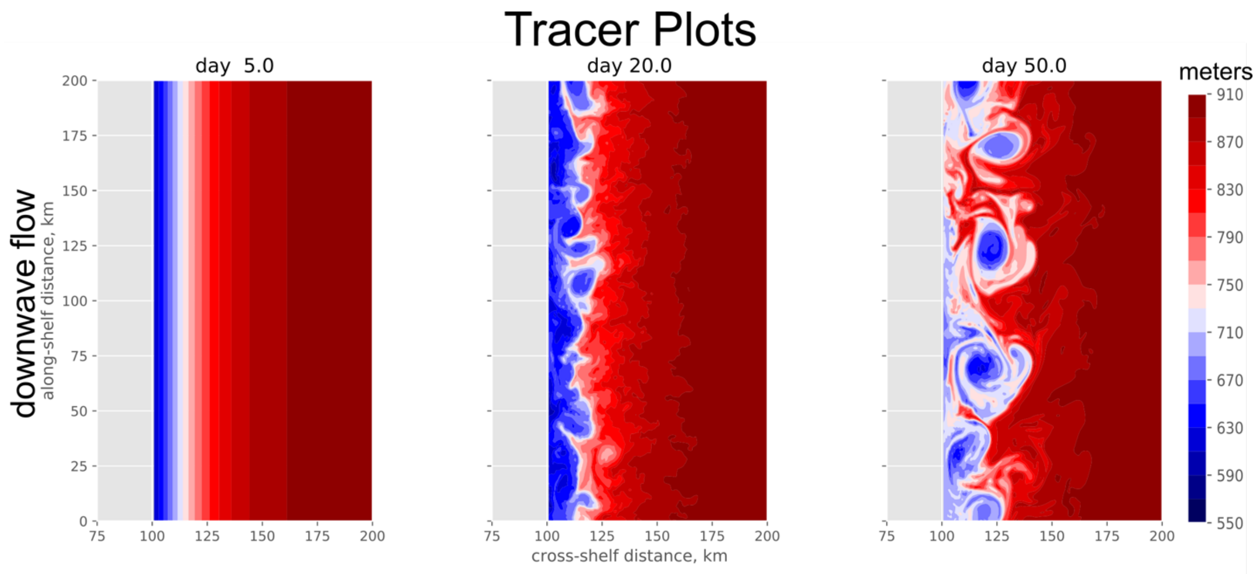

Figure 3: **figTracer:** The model run is initialized with a passive tracer whose value is equal to the depth of the isobath over which it starts; its initial value does not vary with either depth or along-shelf position. The tracer is shown at 600m depth on day 5, 20, and 50 for initial flows of 30 cm/s in the downwave direction. N=0.005 s^{-1}, f=10^{-4} s^{-1}, r=5x10^{-4} m s^{-1} and S=0.5 in both cases.

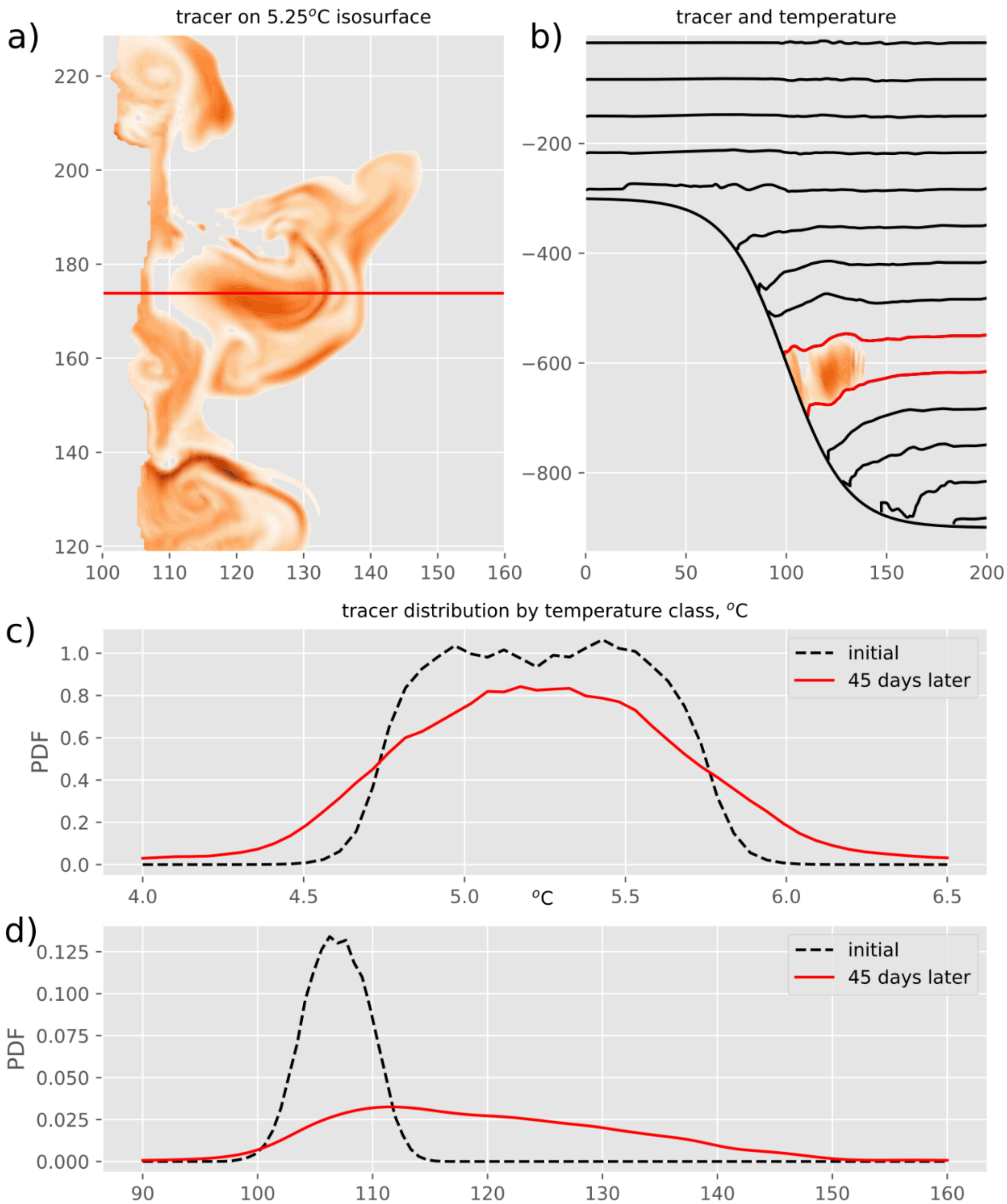

Figure 4: **FigTracer:** The evolution over 45 days of a tracer introduced into the base model, S=0.5, between the 4.75 and 5.75°C isotherms within 50m of the bottom. A) tracer distribution on the 5.25°C isotherm. B) cross-shelf distribution of tracer (color) and isotherms at 175km alongshore (the red line in A). The red isotherms are the 4.75 and 5.75°C isotherms, all isotherms are separated by 1°C. C) the distribution of the tracer in the entire model domain by temperature class at introduction and 45 days later. D) the distribution of the tracer by cross-shelf distance over entire model domain.

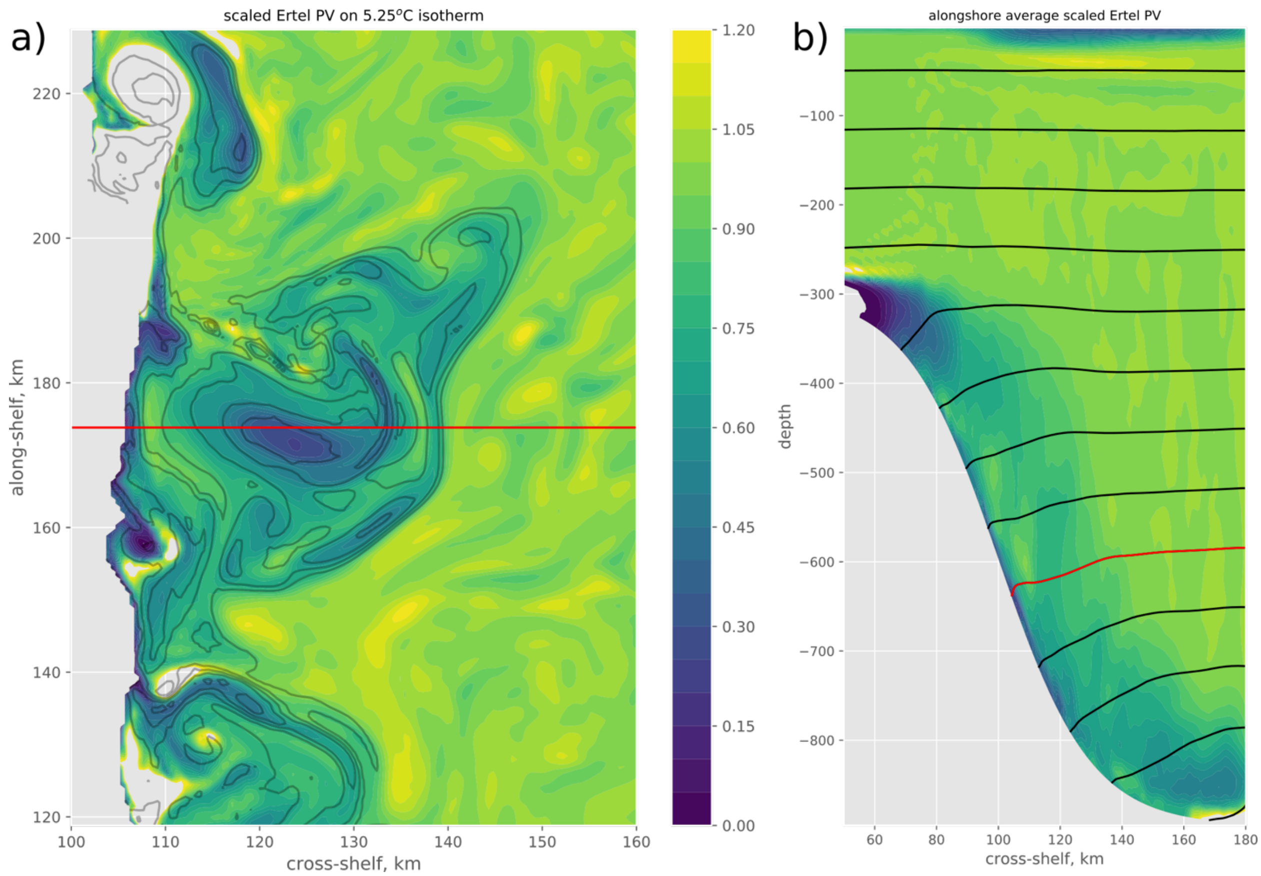

Figure 5: **A)** The potential vorticity computed on the 5.25ºC isotherm scaled by the initial potential vorticity fN_0^2 for the same time and model run as the tracer field shown in figure 4. The grey contours are the tracer field shown in figure 4A; the red line is the position of the slice shown in figure 4B. **B)** The alongshore averaged potential vorticity scaled by the initial potential vorticity (colors) overlain by the isotherms (black, with 1ºC interval). The red isotherm is the 5.25ºC isotherm.

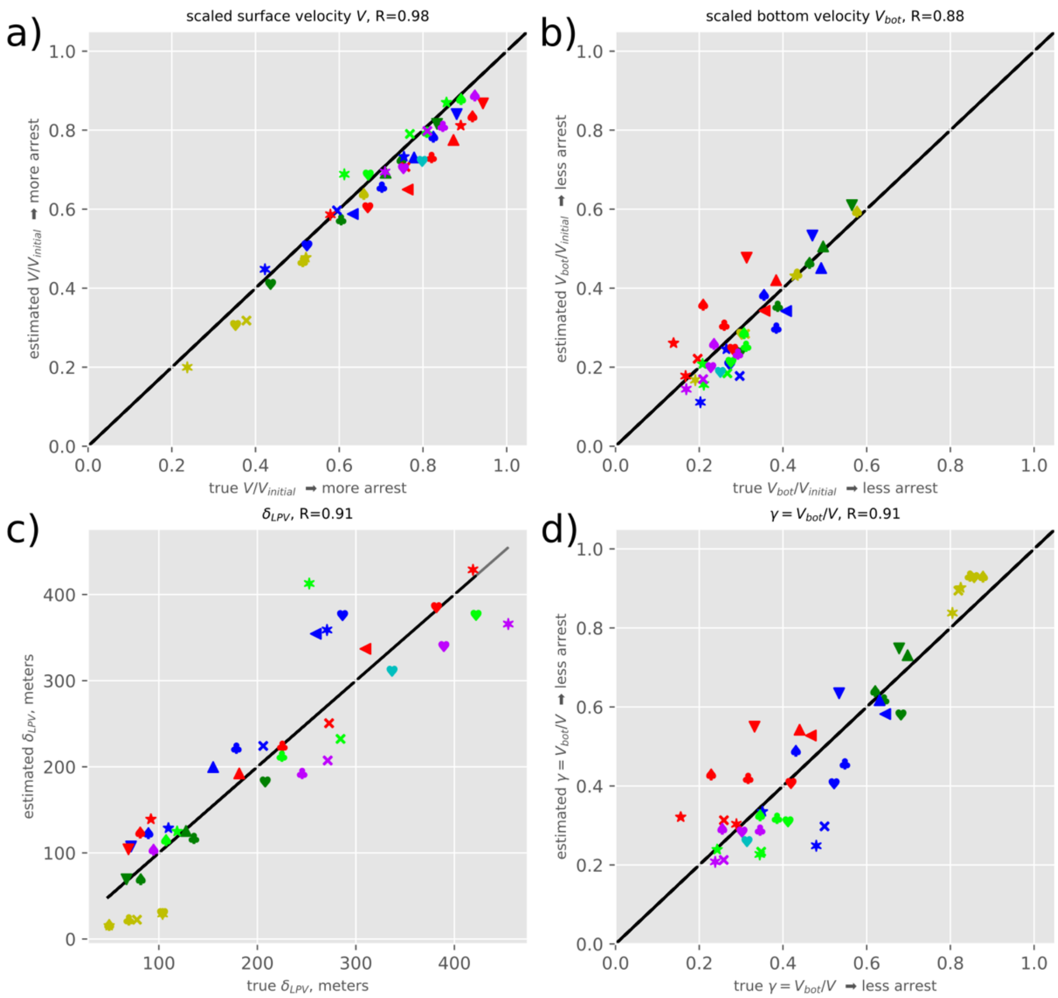

Figure 6: A) The surface velocity scaled by the initial velocity after 30 days for the simple model (the "estimate" on the vertical axis) versus the complete numerical model (the "truth", on the horizontal axis) in day 30 of runs made with quadratic bottom friction. B) A comparison of the velocity at the bottom scaled by the initial velocity; otherwise as (A). C) A comparison of the thickness of the low-PV layer. D) A comparison of γ, the ratio of the bottom velocity to the surface velocity. A smaller gamma indicates a greater bottom boundary layer arrest. The correlations in the title are Pearson's R, and all are significant (P>0.05). A key to the symbols and colors is given in Table 1.

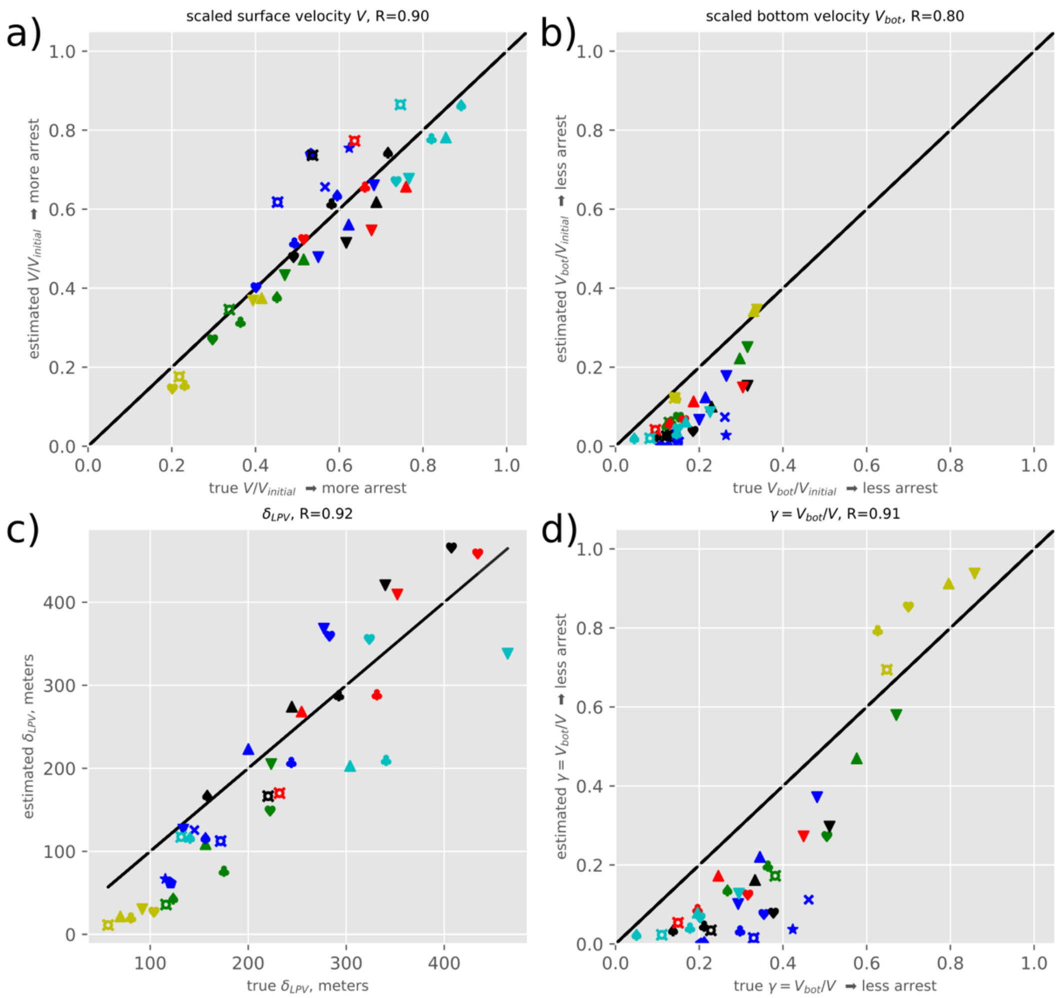

Figure 7: Same as figure 6, but for model runs with linear bottom friction.

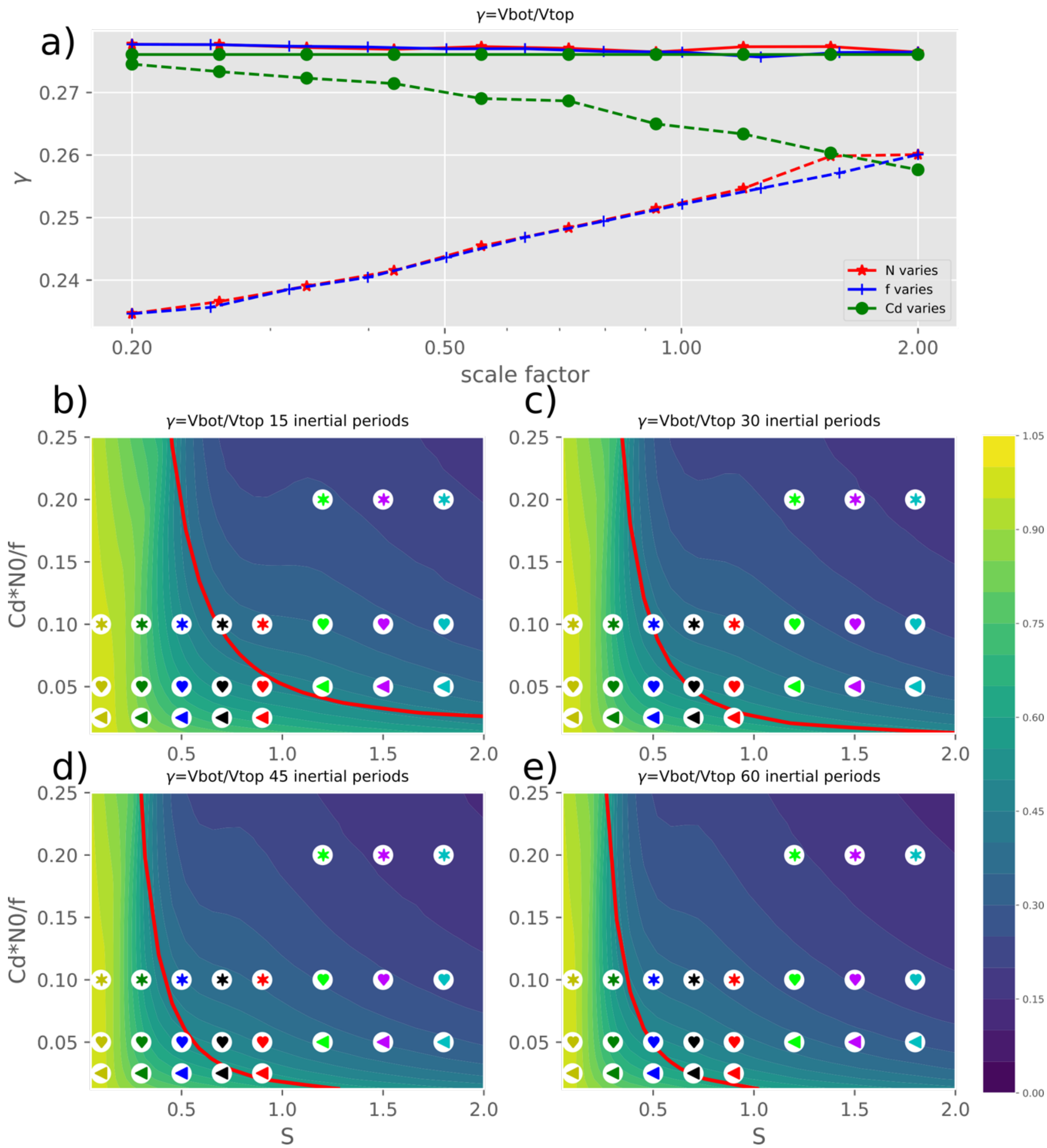

Figure 8: A) The ratio of surface to bottom velocity γ at 30 days for the non-dimensional parameters S=1.0, N/f=50.0, C_dN/f=0.15 and a model run 41.3 inertial periods. Each line represents either N, f, or C_d varying by a factor 0.2 to 2.0 while keeping the non-dimensional parameters constant; the dashed line is for a model run with a depth of 600m, the solid for a model run of effectively infinite depth. Panels B) through E) are γ as a function of S and C_dN/f for 15, 30, 45 and 60 inertial periods. In all, N/f=50.0. The red line indicates where the bottom arrest timescale of Brink and Lentz (2009) matches the modeled time; the arrest time scale is smaller than the modeled time above and to the right of the line. The symbols on the plots correspond to the parameters of the full numerical model runs made with a quadratic drag law, and match the symbols in table 1 and figures 7 and 6.

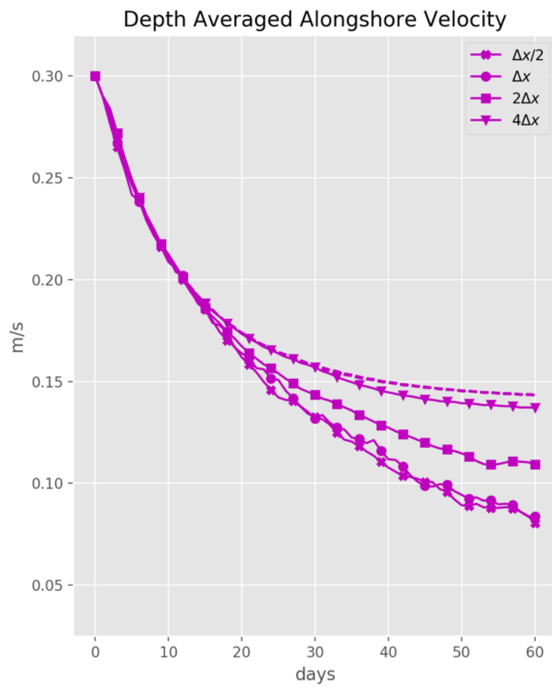

Figure 9**:** The vertical mean alongshore current 100km offshore over the 600m isobath for models with different resolutions, S=0.5 and initial currents of 0.3 m/s with a linear friction of $5\text{x}10^{-4}$ m s^{-1}. The model resolution is indicated as Δx for 500m, Δx/2 for 250m, 2Δx for 1km, and 4Δx for 2km resolution. The dashed line indicate the solutions with no alongshore variation; these have no resolution dependence.

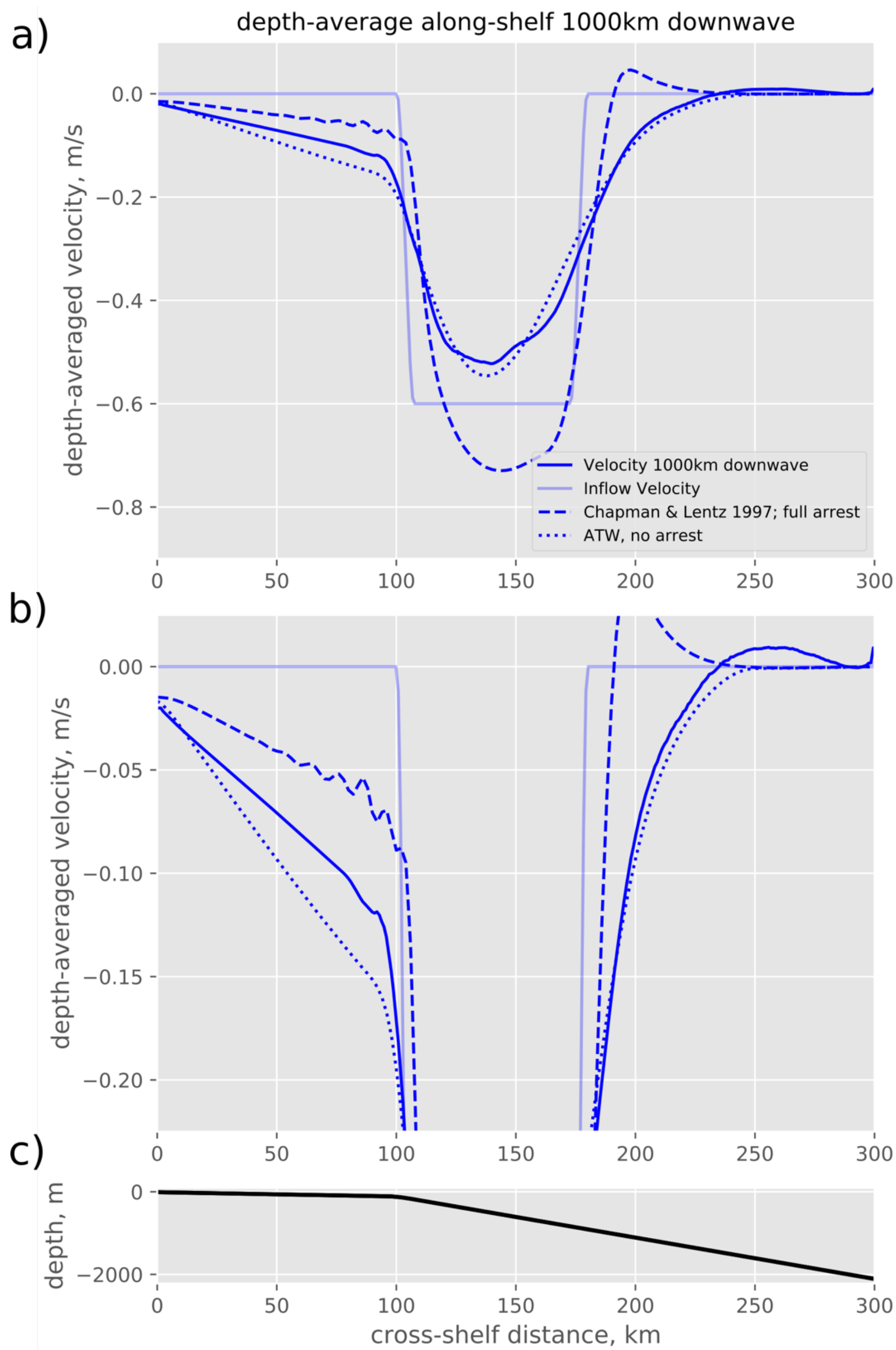

Figure 10: A) The alongshore velocity at the northern boundary (inflow velocity) and 1000km downwave for an inflow of 60 cm/s over the upper slope. Shown are the depth averaged velocities for the numerical model, the Chapman & Lentz (1997) solution with boundary layer arrest, and the unstratified Arrested Topographic wave solution (ATW). B) Same as A, but with the vertical axis enlarged to show the slope flows. C) The bathymetry.

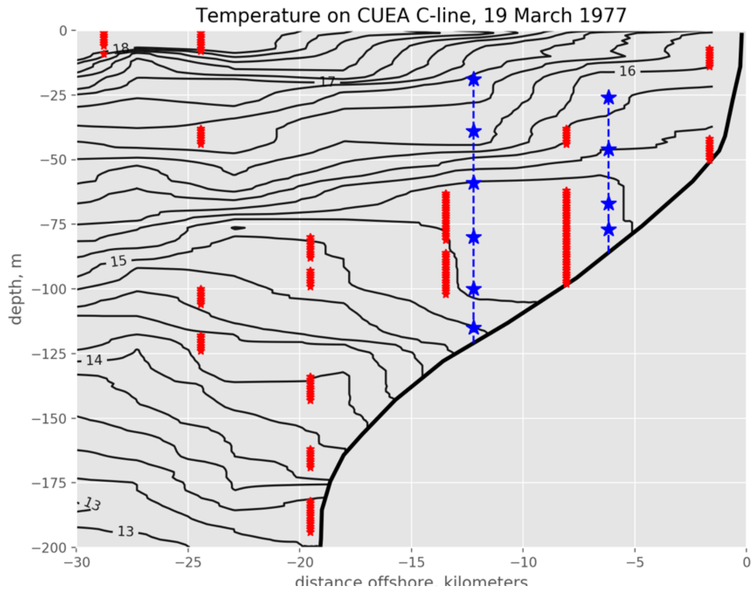

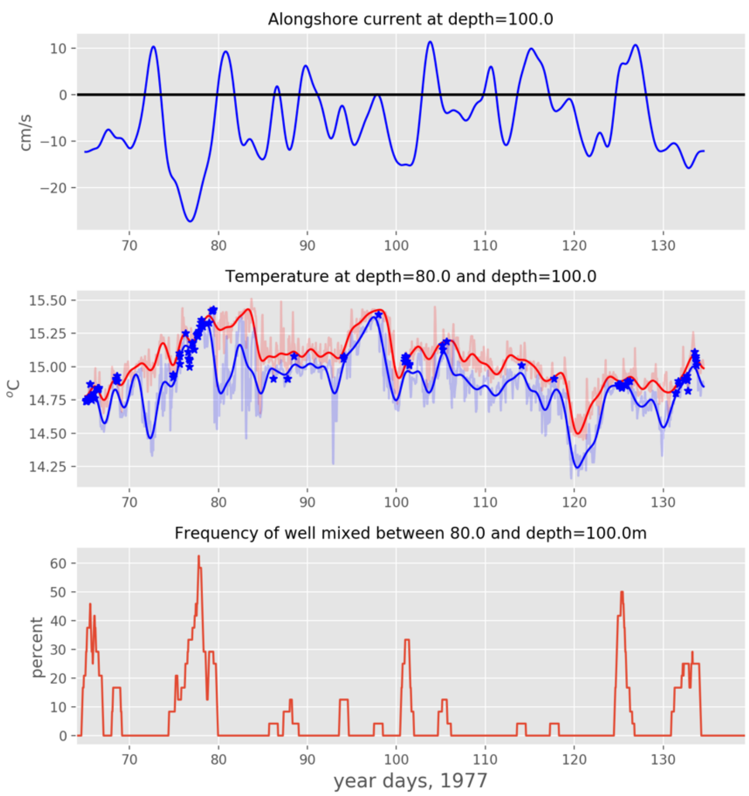

Figure 11: A) A cross-shelf temperature section from the Coastal Upwelling Ecosystem Analysis Program at 15°S in Peru on March 19, 1977. Red stars indicate "well-mixed" (as defined in the text) portions of the water column. Blue lines are stars are moorings. B) the lowpass filtered alongshore current at 100m depth on the 121m isobath (roughly 10km offshore). C) The temperature at that mooring at 80 and 100m depth. The darker lines are low passed, the faded lines are the raw hourly data. Blue stars indicate where the water is "well-mixed." D) The frequency within a day of weakly stratified water detected between the 80 and 100m temperature sensors.

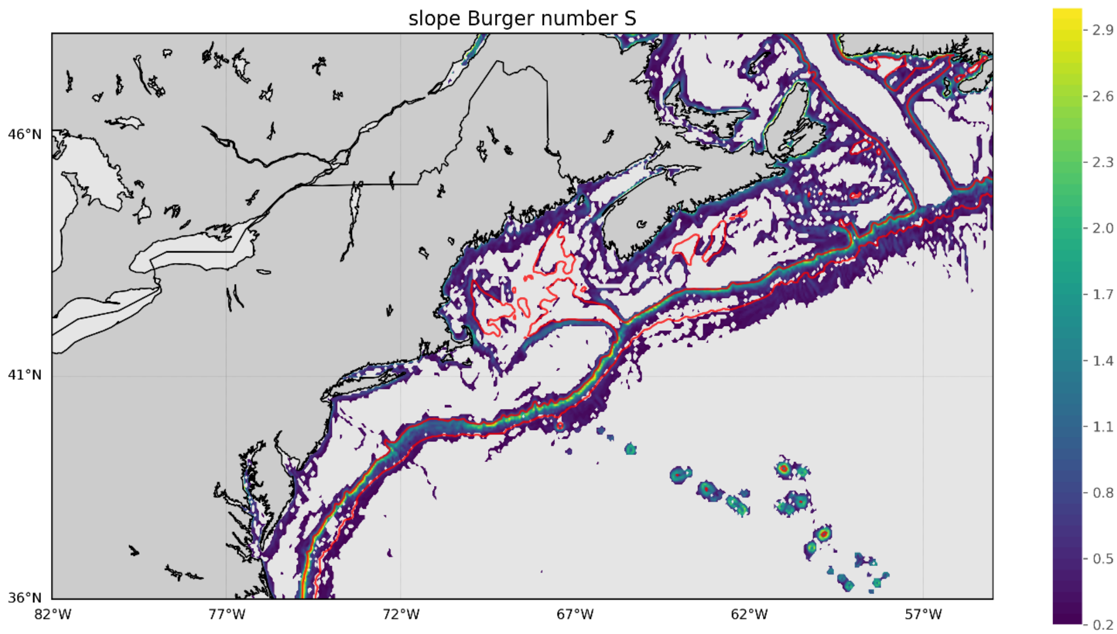

Figure 12: **figBurgerNumber**: The slope Burger number calculated from the Northern Hemisphere World Ocean Atlas hydrography for summer and bottom bathymetry from the STRM15 data set, smoothed by a 7km filter for the Mid-Atlantic Bight shelf/slope systems. The red lines indicate the 200 and 2000m isobaths.